Available online at www.sciencedirect.com
ScienceDirect
Continental Shelf Research 29 (2009) 101–118
CONTINENTAL SHELF RESEARCH
www.elsevier.com/locate/csr

Lateral circulation driven by boundary mixing and the associated transport of sediments in idealized partially mixed estuaries

Shih-Nan Chen*, Lawrence P. Sanford

Horn Point Laboratory, University of Maryland Center for Environmental Science, Cambridge, MD 21613, USA

Received 16 January 2007; received in revised form 31 October 2007; accepted 2 January 2008
Available online 12 January 2008

Abstract

A three-dimensional, hydrostatic, primitive equation numerical model with modern turbulence closures is used to explore lateral circulation and the associated transport of sediments in idealized, moderately to highly stratified estuaries. The model results suggest that boundary mixing on a sloping bottom can drive a significant amount of lateral circulation. This mechanism has received little attention to date in the estuarine literature. Good agreement with an analytical solution and similar vertical structures of lateral flows to observations from the Hudson River estuary support the importance of the boundary mixing mechanism. Boundary mixing is at least as important as differential advection for the modeled scenarios, when the two mechanisms are evaluated using the salt balance equation for model runs without rotation. Linearly superposing analytical solutions for lagged boundary mixing lateral flow and Ekman-forced lateral flow yields a good representation of the near-bottom lateral flow from the model with rotation. The 2 h lag required for the boundary mixing solution is roughly equal to the vertical diffusion time scale, indicating that lateral flow adjustment depends on development of a bottom mixed layer. Sediment dynamics at cross sections seaward and landward of the salt intrusion are very different. Seaward of the salt intrusion, sediments are eroded in the channel and preferentially deposited on the right slope (looking seaward), mainly due to the combination of high sediment concentration in the channel during flood with strong up-slope transport on that side (tidal pumping). Lateral sediment re-distribution landward of the salt intrusion is negligible due to weak residual lateral circulation.
© 2008 Elsevier Ltd. All rights reserved.

Keywords: Lateral circulation; Boundary mixing; Sediment transport; Ekman turning; Estuarine circulation; Numerical modeling

1. Introduction

Lateral circulation in estuaries results in an exchange of water masses in the cross-channel direction. Despite its typically smaller magnitude compared with along-channel flow, lateral circulation is important for transport processes in estuarine environments. As noted by Fischer (1972) and Smith (1980), it can drive along-channel dispersion of salt and other tracers and thus can affect the overall salt budget in estuaries. The salt budget, in turn, determines the along-channel density gradient which ultimately drives estuarine circulation. Lateral circulation can also affect sediment dynamics (Geyer et al., 1998; Woodruff et al., 2001; Huijts et al., 2006; Fugate et al., 2007). Geyer et al. (1998), for example, observed a turbidity-maximum zone skewed toward the west side of the Hudson River estuary. Such cross-channel variations were explained by the convergence of lateral flows.

There are various mechanisms that can potentially drive lateral circulation in estuaries. For a straight and stratified estuarine channel, potential driving mechanisms (following the terms defined by Lerczak and Geyer, 2004) are: interactions between barotropic tides and cross-channel variations in bathymetry (Li and O'Donnell, 1997; Li and Valle-Levinson, 1999; Valle-Levinson et al., 2000), Coriolis forcing (Kalkwijk and Booij, 1986; Johnson and Ohlsen, 1994; Ott and Garrett, 2002), differential advection of along-channel density gradients (Smith, 1980; Nunes and Simpson, 1985; Huzzey and Brubaker, 1988), and boundary mixing on a sloping bottom (Wunsch, 1970; Phillips, 1970). Among these, the boundary-mixing mechanism originally proposed for deep ocean mixing has received the least attention. Lerczak and Geyer (2004) used a

*Corresponding author. Tel.: +1 410 221 8296.
E-mail address: schen@hpl.umces.edu (S.-N. Chen).

0278-4343/$ - see front matter © 2008 Elsevier Ltd. All rights reserved.
doi:10.1016/j.csr.2008.01.001

numerical model to explore the relative importance of the mechanisms described above under varying stratification. They reported that the contribution from boundary mixing is relatively weak, compared with differential advection and Ekman veering in a well-mixed system. There are also very few observations of boundary mixing in estuarine flows, due in part to the required high resolution of the bottom boundary layer. Phillips et al. (1986) reported a persistent lateral flow from the boundary to the interior at mid-depth (near the halocline), which is consistent with the lateral flow patterns driven by boundary mixing. However, due to limited data, the indication was not conclusive.

Recently, discerning the relative importance of these different mechanisms in different systems has received increasing attention. In a straight, homogeneous tidal channel with mild depth variations, Coriolis forcing that drives lateral flows by veering of the mean along-channel current in the bottom Ekman layer dominates lateral dynamics (e.g. Mied et al., 2002). Differential advection of along-channel density gradients that sets up transverse density gradients and drives bottom divergent lateral flows during flood has been argued to govern lateral dynamics in vertically mixed systems (Lerczak and Geyer, 2004). In estuaries with strong vertical stratification, however, the main driving mechanisms are less clear.

In this paper, our objectives are (1) to demonstrate that boundary mixing on a sloping bottom can be an important mechanism to drive lateral circulation in moderate to highly stratified estuaries and (2) to explore the associated transport of sediments. Following the approach of Lerczak and Geyer (2004) but using modern turbulence closures, we use a numerical model to investigate lateral dynamics. This paper is organized in the following manner: the boundary mixing process on a slope is reviewed in Section 2. The numerical model is described in Section 3. In Section 4, evidence is provided for the importance of lateral circulation driven by boundary mixing on a sloping bottom. In Sections 5 and 6, temporal and spatial variations in flow structure and in sediment dynamics are presented, followed by discussion and conclusions in Section 7. Comparison of boundary mixing and differential advection as drivers of lateral circulation is deferred to Section 7.1.

2. Boundary mixing on a sloping bottom

In a stratified basin with a sloping bottom, isohalines near the bottom have to be perpendicular to the slope so that net salt flux vanishes at the boundary (no-flux boundary condition):

$$k\frac{\partial\rho}{\partial n}\bigg|_{z=-H}=0, \tag{1}$$

where k is eddy diffusivity (assumed to be non-zero), n is the direction normal to the slope, and ρ is the density of fluid. The tilted isohaline near the bottom then sets up a baroclinic pressure gradient that drives up-slope flows (Wunsch, 1970; Phillips, 1970; Weatherly and Martin, 1978) (Fig. 1). The simplest case is without Coriolis forcing as shown in Fig. 1a, where up-slope flows require compensating return flows from boundary to interior, tending to destratify the fluid. This process occurs during both tidal phases, often forming persistent counter-rotating cells. Including Coriolis forcing adds another layer of complexity. As Fig. 1b shows, during ebbs the isohalines are tilted opposite to the surface tilt, and the ebbing currents induce an up-slope Ekman flow on the left slope looking toward the ocean (down-slope Ekman flow on the right). As a result, up-slope flows on the left are strengthened as the boundary-mixing-driven (denoted by V_B in Fig. 1b) and the Ekman-driven (denoted by V_E) flows act in concert, whereas up-slope flows on the right are weakened.

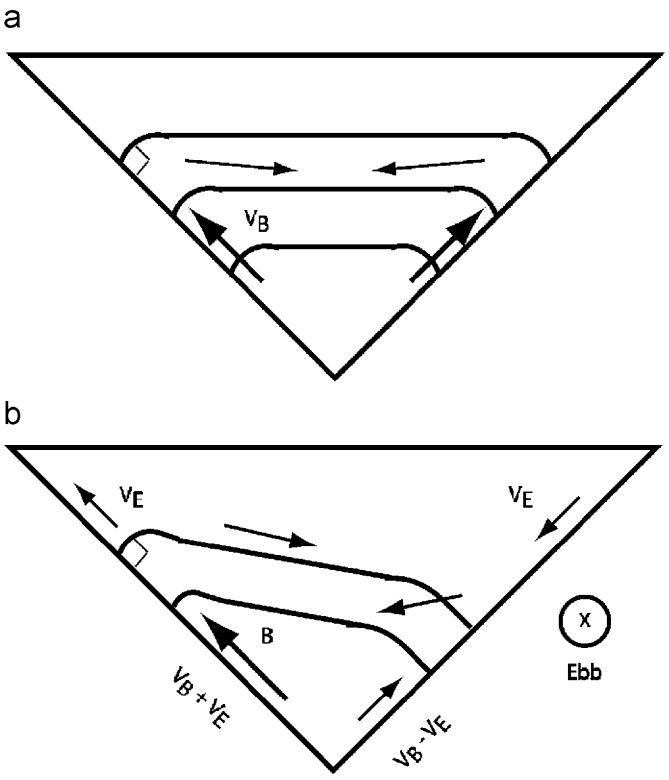

Fig. 1. Schematic diagram of lateral circulation (a) without and (b) with Coriolis forcing. V_B and V_E denote lateral flows driven by boundary mixing and by bottom Ekman veering, respectively. The slope of the triangular channel here is highly exaggerated. In many real estuaries, the cross-channel distance is 2 orders of magnitude larger than the depth.

The interactions between the boundary-mixing-driven and Ekman-driven flows also influence mixing in the bottom boundary layer. On the right slope during ebbs, for example, the Ekman-forced, down-slope flows are against the boundary-mixing-driven, up-slope flows, leading to flow convergence and possible static instability (Garrett et al., 1993). As a result, the boundary layer and halocline may get thicker. The thicker bottom boundary layer on the right slope during ebbs is dynamically equivalent to what Lentz and Trowbridge (1991) observed during down-welling-favorable flows on the California shelf. These patterns alternate sides when the tide turns.

Both steady state and time-dependent boundary mixing solutions have been derived and applied to shelf seas by several authors (Wunsch, 1970; Weatherly and Martin, 1978; Trowbridge and Lentz, 1991; MacCready and Rhines, 1993; Garrett et al., 1993). With constant eddy viscosity and a turbulent Prandtl number of one (e.g. Garrett et al., 1993), the maximum (vertically), steady-state, up-slope flow (V_B) near the bottom is

$$V_B \approx 0.64 A_v q \cot\theta, \tag{2}$$

where A_v is eddy viscosity, θ is the angle of the sloping bottom with horizon, and q is equivalent to the inverse boundary layer thickness:

$$q^4 = \frac{1}{4A_v^2}(f^2 + N^2 \sin^2\theta), \tag{3}$$

where f is the Coriolis frequency and N is the background buoyancy frequency. The strength of up-slope flow apparently depends on mixing, stratification in the interior, and the angle of the slope. Time-dependent behavior is important in the stratified interior away from strong boundary frictional effects (e.g. MacCready and Rhines, 1993). However, in subsequent applications of Eqs. (2) and (3) in this paper (for comparison to numerical model predictions), we assume a quasi-steady balance within the bottom boundary layer with slowly varying eddy viscosity and stratification.

3. Numerical model

We use the Regional Ocean Model System (ROMS; Haidvogel et al., 2000) to simulate an idealized estuarine channel. ROMS is a hydrostatic, primitive equation model using a curvilinear grid in the horizontal and a stretched, terrain-following coordinate in the vertical. The model domain mimics an estuary–shelf system (Fig. 2). The size of the shelf sea is 50 km across shelf × 48 km along-shelf with a constant slope from 200 m at the offshore boundary to 1 m at the shoreline. A straight, 3.6-km-wide estuarine channel intersects the shelf and extends from $x = 50$ to 1000 km. The cross section is of triangular shape with a maximum depth of 14 m in the channel and a minimum depth of 1 m on the sides. The grid configuration is 192 (along-channel, x-direction) × 101 (cross-channel, y-direction) × 15 (vertical levels). The vertical levels are stretched to have higher resolution near the surface and the bottom (lowest near bottom vertical resolution is 0.6 m). The section of the estuarine channel from the mouth to 150 km is more highly resolved ($\Delta x \sim 1$ km, $\Delta y \sim 200$ m). Outside of this area, the grid is telescoped toward the river end ($\Delta x \sim 48$ km) to obtain a long channel and along the shelf sea coast ($\Delta y \sim 1.5$ km) to obtain a bigger salt pool on the shelf without increasing computational cost.

The model is forced by M2 tides from the shelf boundaries using the Chapman condition for free-surface and the Flather condition for depth-averaged, boundary-normal velocity (Marchesiello et al., 2001) and by constant freshwater fluxes from the river end. The long channel dissipates tidal energy and thus minimizes reflection of tidal waves, resulting in progressive tides with current amplitude of 0.4 m s^{-1} in the domain of interest. A weak coastal current (~0.05 m s^{-1}) is specified on the shelf to transport the resulting river plume. Temperature is fixed at 15 °C throughout the domain. Salinity at the river end is set to 0, whereas at the shelf boundaries salinity is nudged to an oceanic value of 32. The initial salinity of the shelf water is 32, while the initial salinity of the channel gradually decreases from 32 to 0 from the estuary mouth to the river head. The salt field reaches a steady structure periodically modulated by tides in about 6 days. We found that including a shelf sea in the simulation is beneficial because it avoids specifying estuary mouth boundary conditions that are not known a priori and helps stabilize the salinity structure in the estuarine channel.

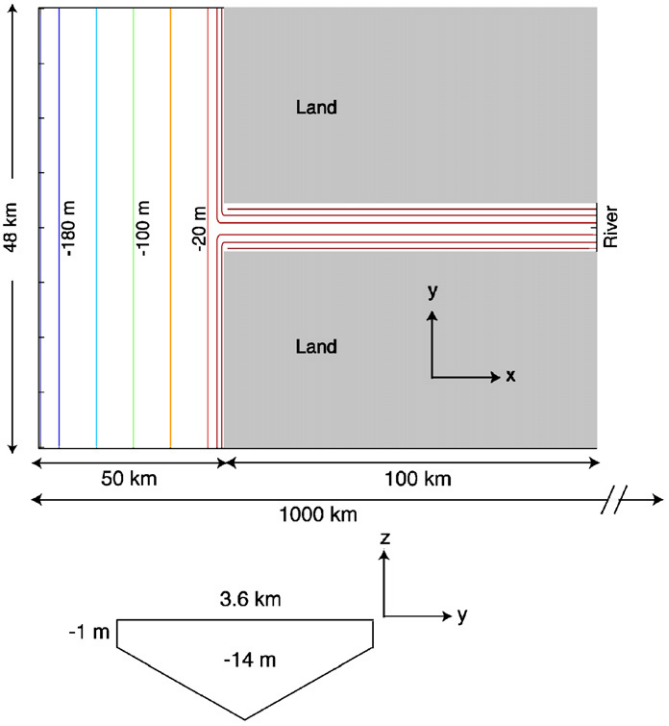

Fig. 2. (a) Plan-view of model domain. The domain mimics a broad continental shelf with a long, straight estuarine channel. The shelf size is 48 km (along-shelf) × 50 km (cross-shelf) with a constant slope from 200 m (off-shelf boundary) to 1 m (land boundary). The estuarine channel extends from $x = 50$ km to about 1000 km. The gray areas are land. Estuarine cross section is plotted in (b). The channel is triangular-shaped and of 3.6 km wide. The deep channel is 14 m, and the shallowest area is of 1 m. Note that the domain is scaled disproportionately for better visualization.

We use the k–ε turbulence closure (Jones and Launder, 1972) with a stability function proposed by Canuto et al. (2001). The k–ε closure has been shown to perform well for estuarine flows (Burchard and Baumert, 1998; Warner et al., 2005b). Bottom stress is computed by assuming a logarithmic velocity profile in the lowest computational cell and a constant bottom roughness parameter (z_0). The

background eddy viscosity and eddy diffusivity are both set to $8\times10^{-5}\,m^2\,s^{-1}$. The reason we use this rather high background value is to obtain a reasonable salt intrusion length ($L=128$ km for the moderately stratified case). Given the relative weak tidal current of $0.4\,m\,s^{-1}$ and freshwater velocity of $0.01\,m\,s^{-1}$, which resembles low-flow conditions in Chesapeake Bay, using a lower background diffusivity of $5\times10^{-6}\,m^2\,s^{-1}$ leads to an unrealistic salt intrusion length of 300 km. While the salt intrusion length is sensitive to background diffusivity, we will show later that the lateral circulation is insensitive to it (Section 4.2).

We also incorporate a single layer, single grain size (0.01 mm silt) sediment bed for exploring lateral transport of sediments (Section 6). The suspended sediment transport module used here was described, implemented, and tested by Warner et al. (2005b) as a part of the Community Sediment Transport Modeling (CSTM) project. Flocculation and bed consolidation are excluded for the sake of simplicity. The sediment bed layer is sufficiently thick so that sediment is never depleted. The erosion formulation is the Ariathurai–Partheniades type, and the deposition formulation assumes no critical stress for deposition (e.g. Sanford and Halka, 1993):

$$E=E_0(1-\phi)\left(\frac{\tau_b}{\tau_c}-1\right),\quad D=w_sC, \tag{4}$$

where E and D are erosion and deposition rate ($kg\,m^{-2}\,s^{-1}$), E_0 is an erosion rate constant ($kg\,m^{-2}\,s^{-1}$), ϕ is the porosity, w_s is the particle settling speed ($m\,s^{-1}$), C is the suspended sediment concentration ($kg\,m^{-3}$), τ_c is the critical shear stress for erosion, and τ_b is the computed bottom stress. Erosion ceases when τ_b is smaller than τ_c. The sediment module is called after flow and salt fields reach a steady state. Model parameters are summarized in Table 1.

To obtain various stratifications, we change the freshwater flux while keeping tidal forcing and turbulence closure the same. Through experimentation, we found that lateral circulation patterns under various stratifications (top–bottom salinity differences from 4.7 to 9.5) are qualitatively similar. Hence, we only show two cases here. The two model runs and some solution characteristics are summarized in Table 2. Cross-sectional averaged freshwater flows of $0.01\,m\,s^{-1}$ (moderately stratified hereafter) and $0.08\,m\,s^{-1}$ (highly stratified hereafter) correspond to salt intrusion length (L) of 126 and 80 km, respectively. The shorter salt intrusion length for the highly stratified case is expected as higher freshwater discharge pushes more salt out of the estuary, given the same tidal forcing. A cross-sectional profile seaward of the salt intrusion is taken at a location about $(3/4)L$ from the mouth (denoted by Slice location in Table 2) for each case. At these two locations, top–bottom salinity differences (ΔS) are 4.7 and 9.5 psu, respectively, which is within the observed range of partially mixed estuaries (e.g. Dyer, 1997).

The tidally averaged salinity structure along the channel for the moderately stratified case, shown in Fig. 3a as an example, is consistent with the salt structure of a partially mixed estuary. The solid vertical line denotes the location where a cross-sectional profile is taken ($(3/4)L$), and the vertical profile of tidally averaged velocity in the channel at

Table 1
Model parameters

Parameters	
Bottom roughness parameter, z_0 (mm)	0.5
Settling speed, w_s ($mm\,s^{-1}$)	0.3
Critical shear stress, τ_c (Pa)	0.05
Erosion rate constant, E_0 ($kg\,m^{-2}\,s^{-1}$)	5×10^{-5}
Porosity, ϕ	0.9
Background eddy viscosity ($m^2\,s^{-1}$)	8×10^{-5}
Background eddy diffusivity ($m^2\,s^{-1}$)	8×10^{-5}

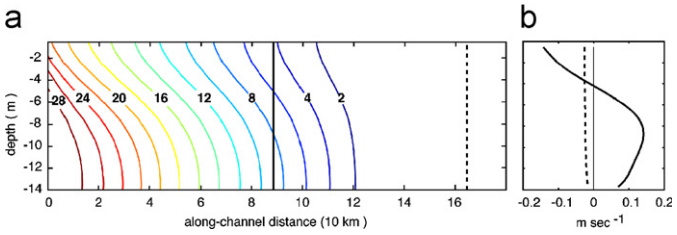

Fig. 3. (a) Tidally averaged salt structure along the channel axis (14 m) starting from the estuary mouth under moderately stratified conditions (model run 1 in Table 2). The solid and dashed vertical lines are the locations where cross-sectional profiles are taken. These two cross sections are referred as seaward of salt intrusion ($\sim(3/4)L$, slice location 90 km in Table 2) and landward of salt intrusion (slice location 163 km). The distances to the limit of salt (2 psu) from these two cross sections are both roughly equal to five tidal excursions. Vertical profiles of tidally averaged along-channel velocity at these two locations are plotted in (b).

Table 2
Model runs and solution characteristics: runs 1 and 2 are the moderately and highly stratified cases, respectively

Run	U_f ($m\,s^{-1}$)	L (km)	Slice location (km)	ΔS (psu)	U_e ($m\,s^{-1}$)	U_t ($m\,s^{-1}$)
1	0.01	126	90 (solid line in Fig. 3)	4.7	0.11	0.37
	0.01	126	163 (dashed line in Fig. 3)	0	N/A	0.29
2	0.08	80	60	9.5	0.20	0.42

The first row of run 1 is the solution characteristics seaward of the salt intrusion, and the second row is landward of the salt intrusion. U_f is the freshwater velocity; L is the salt intrusion length defined as the distance between the mouth to 2 psu; ΔS is the top–bottom salinity difference in the channel; U_e is the rms amplitude of estuarine circulation; and U_t is the tidal current amplitude at the given cross section.

(3/4)L (Fig. 3b) shows a reasonable estuarine circulation with landward flow near bottom and seaward flow near surface. The dashed vertical line in Fig. 3a is where another cross-sectional profile is taken upstream of the limit of salt (see Table 2). As expected, the corresponding tidally averaged velocity (Fig. 3b) shows seaward transport over the entire water column.

4. Lateral circulation driven by boundary mixing

In this section, we will show lateral circulation patterns and their comparisons with an analytical model and observations for both moderately and highly stratified cases (model runs 1 and 2). We aim to demonstrate that boundary-mixing-driven lateral circulation is robust.

4.1. Circulation patterns

Without Coriolis forcing, circulation patterns are symmetric about the channel axis, and near-bottom up-slope flows are equal on both sides. In Fig. 4a, two counter-rotating cells on either side of the channel axis are evident at 2 h after maximum flood for the moderately stratified ($U_f = 0.01$) case without Coriolis forcing. The isohalines in the interior are flat but are distorted upward before intersecting the sloping bottom at a right angle (the contours in the figures do not appear perpendicular to the boundary because of vertical exaggeration). The up-slope flows and the isohalines perpendicular to the slope are consistent with the boundary mixing mechanism proposed by Wunsch (1970) and Phillips (1970) (Fig. 1a). The magnitude of maximum lateral current (v) is about 4 cm s^{-1}, whereas the maximum vertical current (w) is about 0.025 cm s^{-1}. Flow returns (down-slope) near the top of bottom boundary layer. This is partly due to gradual decreases of boundary mixing from the channel to shallow region (vanishes about 3 m below surface), gradually weakening the up-slope flows. The weakening thus leads to flow convergence along the slope, forcing boundary water to move to the interior. This mechanism, known as tertiary flow, was demonstrated in laboratory experiments by Phillips et al. (1986). The other reason may be the baroclinic pressure gradient generated by up-slope flow itself. The up-slope flow tilts the flat isohaline upward, which creates a baroclinic force to drive flow from boundary to the interior (Garrett et al., 1993).

Including Coriolis forcing induces axial asymmetry, and the resulting circulation appears to be a superposition of boundary-mixing-driven and Ekman-forced flows. For the moderately stratified case at 2 h after maximum flood (Fig. 4b; model run 1 in Table 2), up-slope flows can still be seen on both slopes but are stronger on the right slope than on the left. The strengthened lateral flows on the right slope have a maximum magnitude of about 4.7 cm s^{-1}. The circulation pattern is complex and resembles the superposition of the circulation pattern without Coriolis forcing (Fig. 4a) and a counter-clockwise circulating cell. The counter-clockwise circulation is consistent with bottom

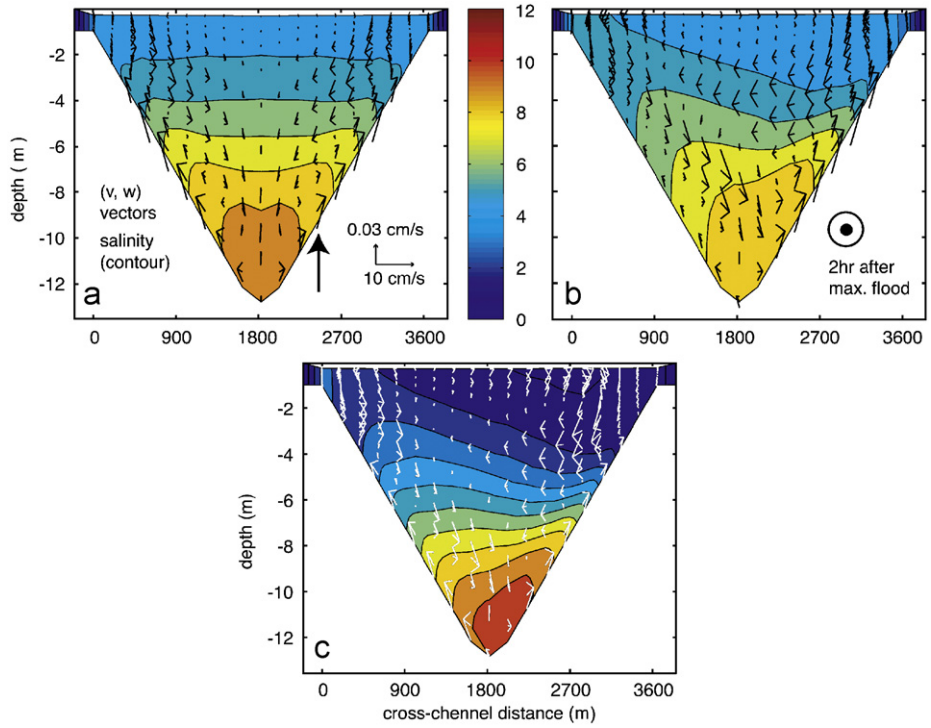

Fig. 4. Cross-sectional profiles of salinity (contoured) and lateral circulation (vectors) for (a) moderately stratified without Coriolis forcing, (b) moderately stratified with Coriolis forcing, and (c) highly stratified with Coriolis forcing cases at 2-h after maximum flood. All of the cross-sectional profiles presented in this paper are looking seaward. The arrowhead denotes a location off the channel (depth~10, 0.8 m above the bottom) where time series of lateral flow velocity are obtained.

Ekman-veering during flood with a return flow higher in the water column. The asymmetrical boundary layer thickness about the channel also indicates the interactions between boundary-mixing-driven and Ekman-forced flows. As in Lentz and Trowbridge (1991)'s observations on the California shelf, the bottom boundary layer is usually thicker during downwelling-favorable currents, such as the condition on the left slope in Fig. 4b and c. This is owing to the convergence of up-slope flows driven by boundary mixing and down-slope flows forced by Ekman-veering. Upwelling-favorable conditions appear on the right slope and thus the boundary layer is thinner there.

In the highly stratified case (Fig. 4c), the circulation patterns are similar to the moderately stratified case (Fig. 4b), but the boundary layer is thinner than the moderately stratified case because turbulent mixing is suppressed by the stronger stratification. Also, the influence of a counter-clockwise circulation forced by bottom Ekman-veering is weaker, and the size of the counter-clockwise cell is more confined near the bottom. The weaker Ekman-forced circulation is due to the tilting of isohalines that tends to suppress lateral flow (Chant and Wilson, 1997). Despite the weaker boundary mixing and weaker Ekman-forced flow, the magnitudes of lateral flows (v) do not decrease much with a maximum value of around $3.3\,\mathrm{cm\,s^{-1}}$. One of the reasons is that the increased background stratification (N in Eq. (3)) can sustain the boundary-mixing-driven flow when turbulent mixing is decreased (lower eddy viscosity A_v in Eq. (3)). The above patterns evolve as the tide changes (see Section 5).

4.2. Sensitivity tests and temporal variability without Coriolis forcing

Vertical mixing in stratified fluid is critical to generate the lateral circulation pattern described in this paper. Because this is a difficult process to model, we used different turbulence closures that have been shown to perform well for simulating estuarine flows (Warner et al., 2005b) and refined the vertical resolution to see if the circulation patterns persisted. These tests were carried out for the simplest case without Coriolis forcing. The results showed that the cross-sectional profiles of salinity and lateral circulation at the location of 3/4 salt intrusion length (L) are qualitatively the same. Fig. 5(a), for example, contains four time series of near-bottom up-slope flow at 0.8 m above bottom, at a location off the channel (indicated by the arrowhead in Fig. 4a; about 10 m deep). As can be seen, four time series corresponding to three turbulence closures and lower background diffusivity ($5\times10^{-6}\,\mathrm{m^2\,s^{-1}}$) are nearly identical, except slight variations in the MY 2.5 closure and slightly weaker magnitude in the low background diffusivity case. This suggests that the predicted lateral circulation pattern is not due to a specific turbulence closure or numerical artifact.

Positive values in the time series of Fig. 5a show that up-slope flows are persistent throughout different tidal stages. The up-slope flows fluctuate with tides and display a stronger peak at about 2 h after maximum flood (indicated by thin vertical lines) with a weaker one at about 2 h after maximum ebb for the moderately stratified condition. The

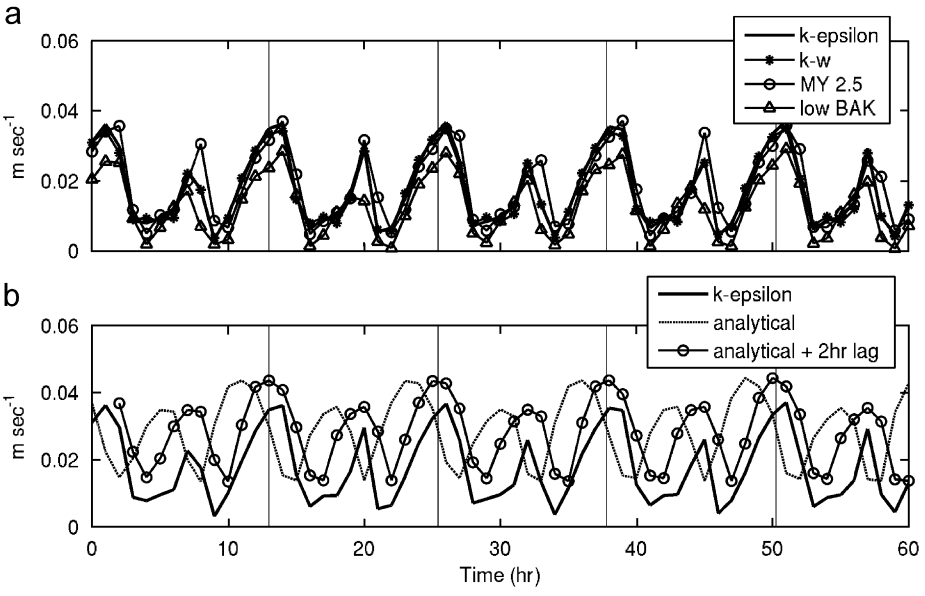

Fig. 5. (a) Comparison of time series of lateral flow velocity with three different turbulence closures and a run with lower background diffusivity of 5×10^{-6} (triangle) under the moderately stratified condition and without Coriolis forcing. In (b), under the same forcing, time series of lateral flow predicted by the model with k–ε closure (thick solid line) are plotted against an steady state analytical solution of boundary-mixing-driven flows using tidally varying eddy viscosities from the model without a 2-h lag (V_B: dashed line) and with a 2-h lag (V_B+2 h lag: thin solid line). The vertical lines are about 2-h after maximum flood. Noted that the time series are taken at the off-channel location indicated by the arrowhead in Fig. 4 at 3/4 of the salt intrusion length. Positive values are up-slope.

persistent up-slope transport is what we expect from lateral flows driven by boundary mixing because the density gradient set up by boundary mixing is always directed from the high salinity channel to the low salinity, shallow flanks. Two peaks in a tidal cycle are due to enhanced mixing associated with maximum flood and ebb currents. The peak after maximum flood is higher because the flooding tidal current and estuarine circulation act in concert. The 2 h lag is likely the result of the lag in vertical mixing of density following maximum floods and ebbs (see Section 7.3 for further discussion). It should be noted that the model results described above are insensitive to our choice of location on the slope, within the stratified region.

A steady state, analytical solution without Coriolis forcing for boundary-mixing-driven flow with a 2 h lag agrees reasonably well with the model results. We apply Eqs. (2) and (3) with instantaneous eddy viscosities from the model at the same location off the channel. As Fig. 5b shows, without a 2-h lag the up-slope flow calculated from the analytical solution peaks at maximum floods and ebbs when turbulent mixing is most energetic. With a 2 h phase-shift, the analytical solution corresponds to the model result reasonably well, and the correlation coefficient is about 0.87. The analytical solution tends to overestimate the up-slope flow. This is associated with the assumption of constant eddy viscosity in the analytical solution. Nevertheless, the reasonable agreement between model results and the analytical solution strongly suggests that boundary mixing is the driving mechanism for the lateral circulation shown here.

4.3. With Coriolis forcing: linear superposition of boundary-mixing-driven and Ekman-forced lateral flows

As mentioned in Section 4.1, superposition of boundary-mixing-driven and Ekman-forced lateral flows appears to represent the cross-sectional profile of lateral circulation with Coriolis forcing (Fig. 4b and c). In Fig. 6a and b for the cases with Coriolis forcing, time series of up-slope flow (thick solid lines) show negative values during ebbs, which indicates the influence of Ekman-forced lateral flows (negative; toward left slope during ebb).

To test the simplest possible case of linear superposition, a representation of Ekman-forced lateral circulation is needed. We start with a simple two-layered model, similar to a three-layer model presented by Martin et al. (2005). Fast decay of eddy viscosity above mid-depth allows us to assume that friction terms in the upper-layer, along-channel momentum equation can be neglected. But bottom friction does contribute at the first order to the lower layer, along-channel momentum balance. Essentially, the layered model assumes that lateral dynamics on tidal timescale are mainly geostrophic. In the lower layer, however, bottom friction slows down along-channel flow, leading to imbalance between Coriolis and pressure gradient forces. This ageostrophic component then drives lateral flow in the lower layer, and continuity requires a return flow in the upper layer. An analytical solution of the two-layer model can be found (Martin et al., 2005):

$$U_1 = \mathrm{Re}\left\{\frac{\partial \eta}{\partial x}\frac{gi}{\omega}\, e^{i\omega t}\right\}, \tag{5a}$$

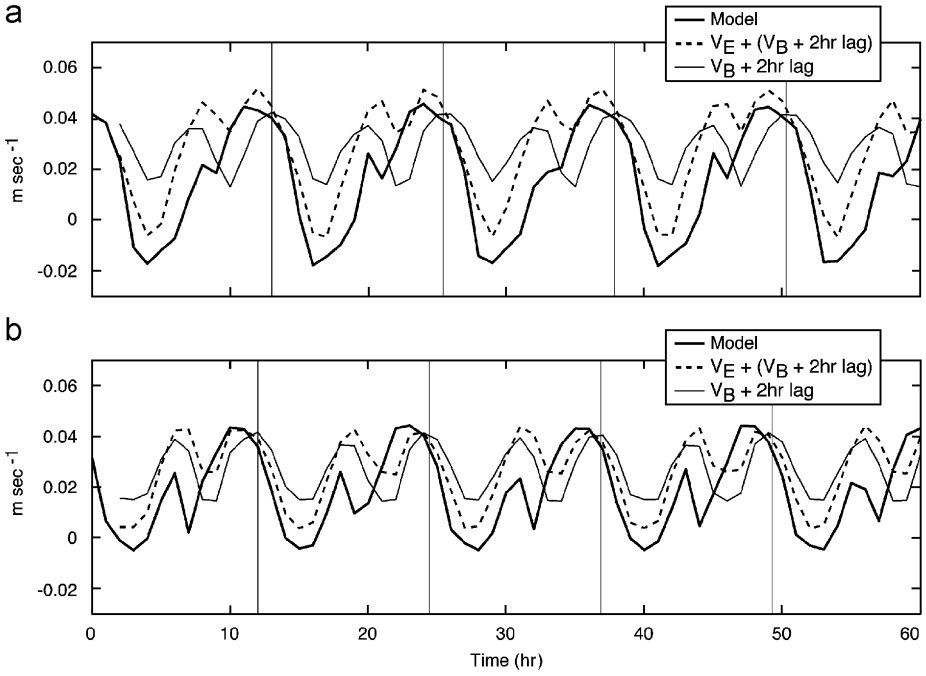

Fig. 6. Time series of lateral flow speed at the same location as in Fig. 5 under the (a) moderately stratified and (b) highly stratified conditions when Coriolis forcing is included. The thick solid lines are the model results. The thin solid lines are the analytical solutions for boundary mixing with a 2-h lag (V_B+2 h), whereas the dashed lines are linear superposition of two analytical solutions accounting for boundary-mixing-driven and Ekman-forced lateral flows ($V_E+(V_B+2$ h)).

$$U_2 = \mathrm{Re}\left\{\frac{\partial\eta}{\partial x}\frac{g}{\omega}\frac{(\mathrm{i}-R/\omega)}{(1+R^2/\omega^2)}\,\mathrm{e}^{\mathrm{i}\omega t}\right\}, \tag{5b}$$

$$V_{E1} = \mathrm{Re}\left\{\frac{1}{2}\frac{\partial\eta}{\partial x}\frac{Rfg}{h_1 g'\omega}\frac{(\mathrm{i}-R/\omega)}{(1+R^2/\omega^2)}y(W-y)\,\mathrm{e}^{\mathrm{i}\omega t}\right\}, \tag{5c}$$

$$V_{E2} = \mathrm{Re}\left\{-\frac{1}{2}\frac{\partial\eta}{\partial x}\frac{Rfg}{h_2 g'\omega}\frac{(\mathrm{i}-R/\omega)}{(1+R^2/\omega^2)}y(W-y)\,\mathrm{e}^{\mathrm{i}\omega t}\right\}, \tag{5d}$$

where subscripts 1 and 2 denote upper and lower layer, U and V_E are along-channel and cross-channel (lateral) velocity, respectively, $\partial\eta/\partial x$ is the prescribed barotropic tidal forcing, g is gravitational acceleration, g' is reduced gravity, h is layer thickness, y is cross-channel coordinate, W is channel width, ω is M2 tidal frequency, and R is a Raleigh drag factor. R is expressed by Geyer et al. (2000) as

$$R \approx \frac{2C_D U_T}{h_2}, \tag{6}$$

where U_T is the rms along-channel tidal velocity at 2.5 m above bottom, and the drag coefficient ($C_D = 0.0022$) can be obtained by assuming a logarithmic velocity profile with known bottom roughness parameter (0.5 mm in Table 1) and reference height of 2.5 m. General solution characteristics are described in Martin et al. (2005). Solutions for lateral flow (Eqs. (5c) and (5d)) are consistent with bottom Ekman-veering in the lower layer and an opposite-directed, return flow in the upper layer (counter-clockwise circulation during flood, looking seaward). Isohalines tilted against sea-surface slope in the cross-channel direction also qualitatively match the model results (Fig. 4b and c). It should be noted that a phase difference between the upper layer axial flow and all other flow components resulting from bottom friction is implicit in the solution (see Section 7.3 for further discussion).

To capture first-order effects, we apply this analytical solution to a simple rectangular cross section with layer thickness roughly equal to model results shown in Fig. 4b and c ($h_1 = 5$, $h_2 = 9$). The reduced gravities (g') are 0.028 and 0.057 for moderately and highly stratified cases, respectively. The barotropic pressure gradient is chosen to have along-channel velocity of 0.4 m s^{-1} in the upper layer. The resulting Ekman-forced lateral flow in the lower layer (V_{E2}) reaches largest amplitude (2.2 and 1.2 cm s^{-1} for these two cases) close to maximum along-channel velocity in the lower layer (U_2). The predicted weaker V_{E2} under the highly stratified condition is consistent with our observation from Fig. 4 that stratification tends to suppress lateral Ekman flows (g' in the denominator in Eq. (5d)). The lower layer in the two-layer model may be considered as the deep channel in the numerical model from a dynamical standpoint. Thus, peak Ekman-forced lateral flow corresponds to peak along-channel lower layer velocity in the channel.

Linear superposition of the analytical boundary-mixing-driven and Ekman-forced lateral flows is a good representation of the numerical model results. In Fig. 6a and b, analytical solutions of boundary-mixing-driven flow alone (V_B; Eq. (2)) and the linear superposition model ($V_B + V_{E2}$; Eqs. (2) and (5d)) are plotted against the model solutions with Coriolis forcing for both stratified conditions. As can be seen, boundary mixing (V_B; thin solid lines) alone cannot explain all the variabilities with correlation coefficients of 0.39 and 0.41. Adding Ekman-forced lateral flow (dashed lines) improves the correlation to 0.88 and 0.69. As Fig. 5 shows, peak boundary-mixing-driven flows lag maximum tidal currents about 2 h, whereas Ekman-forced flows peak at around maximum tidal currents in the lower layer (positive value during flood). This mismatch of phase and the relative strength of V_B and V_{E2} controls the near-bottom lateral flows. The residuals between the analytical superposition and the full model solution mainly come from the overestimation of boundary-mixing-driven flow using Eq. (2), as shown in Fig. 5b. When we replace V_B by the model-predicted boundary-mixing-driven flows (thick solid line in Fig. 5b), the correlation coefficients are close to 1 ($R^2 = 0.97$ and 0.98). Nevertheless, the good representation by the linear superposition model provides additional support for the potential importance of boundary mixing on lateral dynamics in stratified estuaries.

5. Temporal and spatial variations of flow structure

In this section, we will compare tidal variations of flow structures at two locations for the moderately stratified case. These two locations (solid and dashed vertical lines in Fig. 3a) represent transport patterns seaward and landward of the salt intrusion (first and second row of model run 1 in Table 2). They are sufficiently far (~5 × tidal excursion) from the limit of salt to be unaffected by the changing axial gradients near the longitudinal convergence zone.

5.1. Seaward of the salt intrusion

Interactions between boundary-mixing-induced up-slope flow, Ekman-veering, and estuarine circulation exert different controls on near-bottom lateral flows at different tidal phases. Maximum lateral and vertical velocities are around 5 and 0.03 cm s^{-1}. During maximum flood and ebb (Fig. 7a2 and c2), lateral circulation largely resembles Ekman-forced counter-clockwise and clockwise patterns, respectively, but lateral asymmetry of near-bottom flows induced by boundary mixing is evident (stronger lateral flow on the right slope during flood). When along-channel current speed decreases (Fig. 7b2 and d2), Ekman-forced flow is weakened, and the up-slope flow driven by boundary mixing is strengthened (roughly 2-h lag). This leads to net up-slope flow near bottom on both slopes, especially at 2 h after maximum flood (Fig. 7b2). At 2 h after maximum ebb (Fig. 7d2), the net up-slope flow on the right slope is weak because Ekman veering and up-slope flow driven by boundary mixing nearly cancel each other. Although patterns of near-bottom lateral flow reverse from

flood to ebb, the lateral flows are stronger during flood. This is due to the influence of estuarine circulation. Near bottom during flood, flooding currents are in concert with estuarine circulation, resulting in stronger Ekman-veering (Fig. 7a1) and boundary mixing. The more energetic mixing in turn drives stronger up-slope flows (Fig. 7b1). During ebb, on the other hand, ebbing currents are against estuarine circulation near bottom, leading to weaker Ekman-veering and boundary-mixing-induced flows (Fig. 7c1 and d1).

The lateral tilting of isohalines is consistent with thermal wind balance (Fig. 7). In the upper part of the cross section, isohalines are tilted upward to the left shoal for both flood and ebb because the vertical shear of along-channel velocity does not change sign; $\partial u/\partial z<0$ due to sub-surface maximum of flooding currents caused by estuarine circulation. In the lower part of the cross section, on the other hand, isohaline tilting oscillates with tides as the vertical shear changes sign. This pattern is consistent with the finding of Lerczak and Geyer (2004).

5.2. Landward of salt intrusion

Without the influences of salt, lateral circulation is dominated by bottom Ekman-veering (Fig. 8a1 and b1). Magnitudes of lateral and vertical velocities (0.7 and $0.005\,\mathrm{cm\,s^{-1}}$) are considerably weaker than those seaward

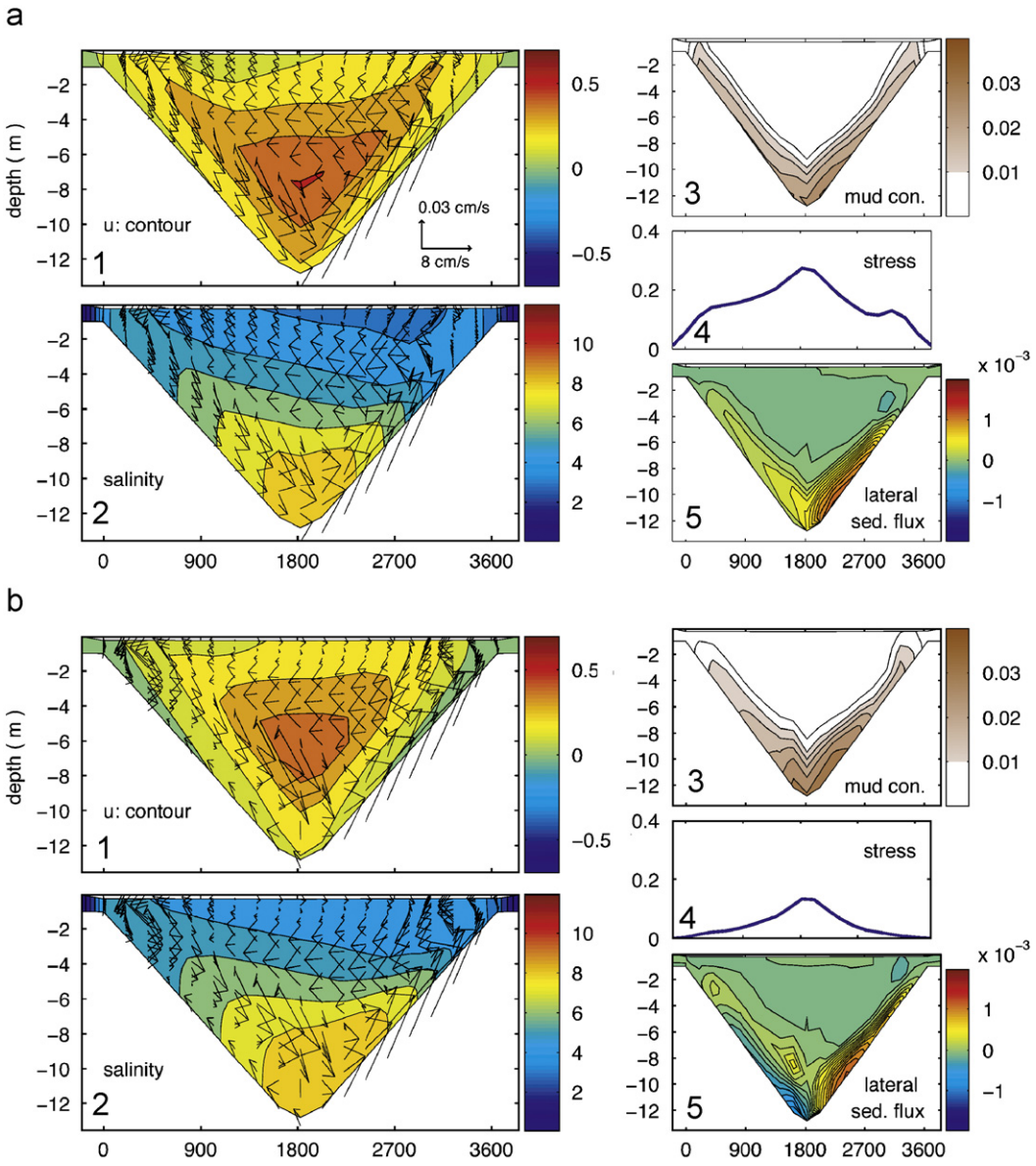

Fig. 7. Cross-sectional profiles of five quantities at the location seaward of the salt intrusion for the moderately stratified case during (a) maximum flood, (b) 2-h after maximum flood, (c) maximum ebb, and (d) 2-h after maximum ebb. Each panel has five figures which are numbered from (1) to (5). The upper left (1) is velocity field (u, v, w). Negative values in the colorbar represent ebbs. The lower left (2) is salinity and (v, w). The upper right (3) is suspended sediment concentration ($\mathrm{kg\,m^{-3}}$). The middle right (4) is bottom stress (Pa). The lower right (5) is lateral sediment flux ($\mathrm{kg\,m^{-2}\,s^{-1}}$). Positive values in the color bar represent transport toward the right slope.

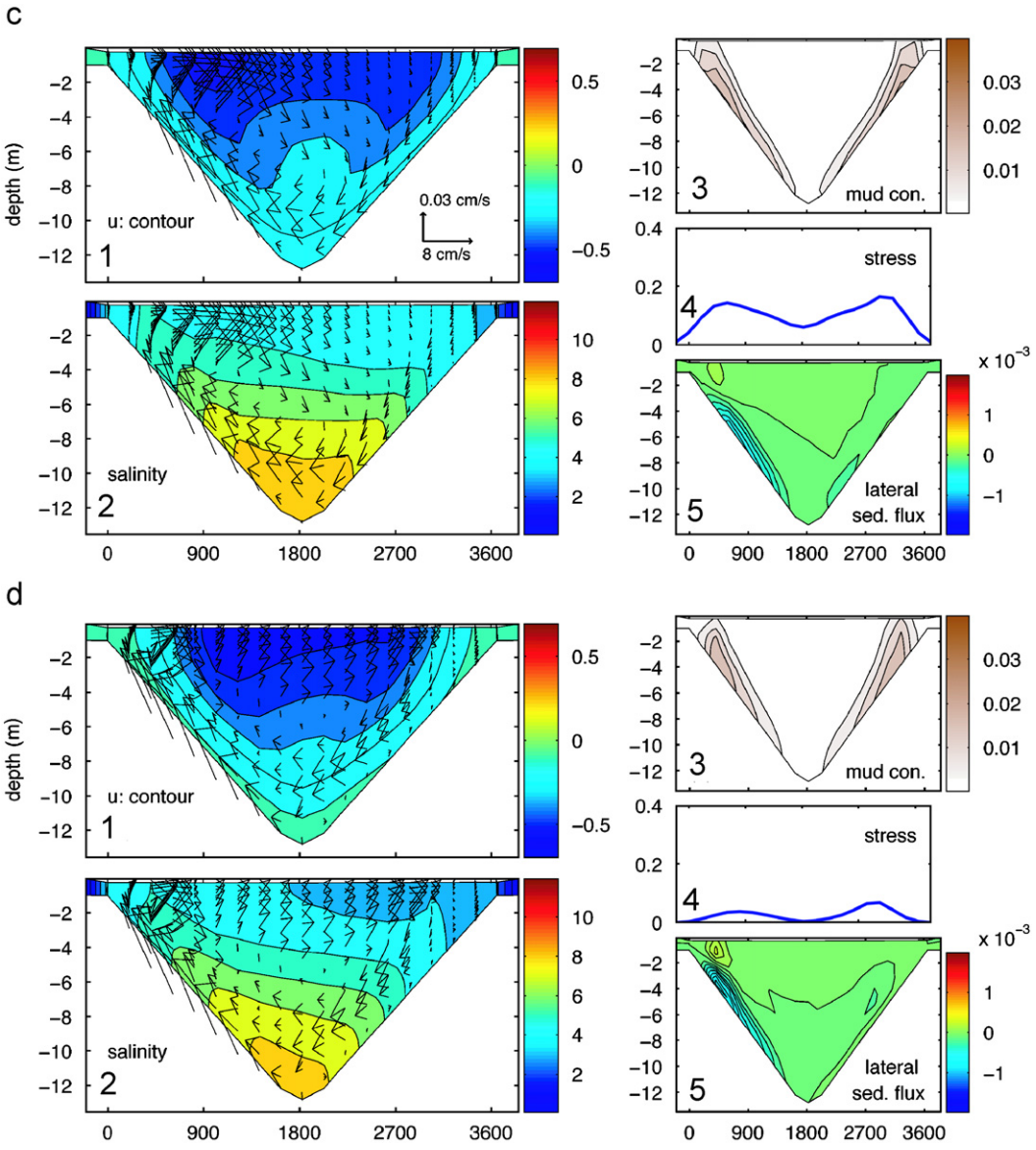

Fig. 7. (*Continued*)

of the salt intrusion due to weaker tidal current and vertical shear that drives Ekman-forced lateral circulation.

6. Implications for sediment dynamics

In this section, tidally varying and tidally averaged sediment transport patterns at two cross-sections for the moderately stratified case (same as in Section 5) are compared.

6.1. Tidally varying sediment dynamics

Seaward of the salt intrusion, estuarine circulation has a strong impact on sediment dynamics. During ebb, near bottom currents in the channel are weakened by the opposing estuarine circulation. Therefore, bottom stress in the channel is relatively low (Fig. 7c4 and d4). During flood, on the other hand, tidal currents and estuarine circulation are in concert, resulting in peak bottom stress in the channel (Fig. 7a4 and b4). Such tidal asymmetry in bottom stress causes high suspended sediment concentrations in the channel during flood and on the slopes during ebb (Fig. 7a3–d3). Noticeably, there are two secondary bottom stress peaks around depth of 4 m in Fig. 7a4, c4, and d4. This is due in part to the relatively weak stratification above this depth. The combination of near-bottom lateral flows and tidally asymmetrical suspended sediment distribution then controls the lateral sediment fluxes in Fig. 7a5–d5.

In contrast, landward of the salt intrusion bottom stresses at maximum flood and ebb (Fig. 8a4 and b4) both peak in the channel but are slightly higher at ebb because the freshwater discharge strengthens ebbing currents. As a result, suspended sediment concentration is highest in the channel, and the distributions are similar on flood and ebb

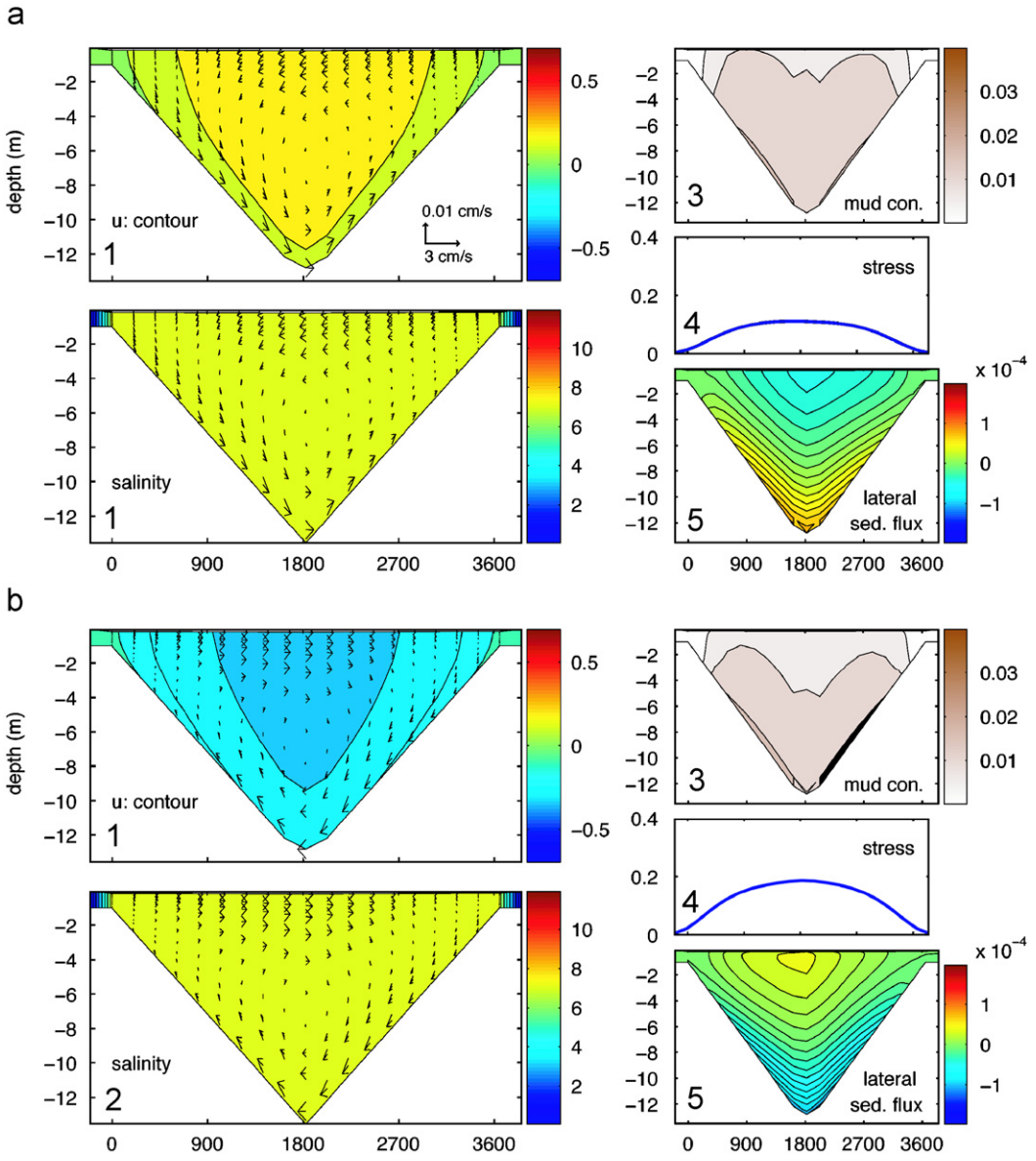

Fig. 8. Same as Fig. 7, but the cross section is at the location landward of salt intrusion and only (a) maximum flood and (b) maximum ebb are plotted. Lateral sediment flux is 1 order of magnitude smaller than that in Fig. 7. Salinity at this tidal fresh cross section (0) is offset by 7.5 for better visualization.

(Fig. 8a3 and b3). Due to the absence of stratification, suspended sediments occupy the whole water column, contrasting with the rather confined vertical distribution seaward of the salt intrusion (e.g. Fig. 7a3). Lateral sediment flux (Fig. 8a5 and b5) is 1 order of magnitude smaller than that seaward of the salt intrusion mainly due to weaker lateral circulation. In the absence of salt and without tidal asymmetry in stress and sediment concentration, lateral sediment flux is thus controlled by Ekman-forced near-bottom lateral flows, which is toward right slope during flood and reversed during ebb.

6.2. *Tidally averaged transport*

The profile of tidally averaged along-channel velocity seaward of the salt intrusion (Fig. 9a), as expected, has the structure of estuarine circulation, whereas landward of salt intrusion the flow is down-estuary (Fig. 9b) and its cross-sectional average is equal to freshwater velocity ($U_f = 0.01$). Seaward of the salt intrusion, the tidally averaged, cross-sectional averaged eddy viscosity is about 4×10^{-4}, yielding an Ekman number of 0.02. An Ekman number less than 1 indicates weaker frictional influences than Coriolis forcing. Thus, the along-channel residual flow is vertically segregated with up-estuary flow near bottom and down-estuary flow near surface, as suggested by Kassi et al. (2000).

In the upper part of the water column, isohalines are predominantly tilted upward toward the left (Fig. 9c), consistent with an approximate thermal wind balance with the vertical shear. However, the tidally averaged, down-estuary surface flow maximum in Fig. 9a is on the left side

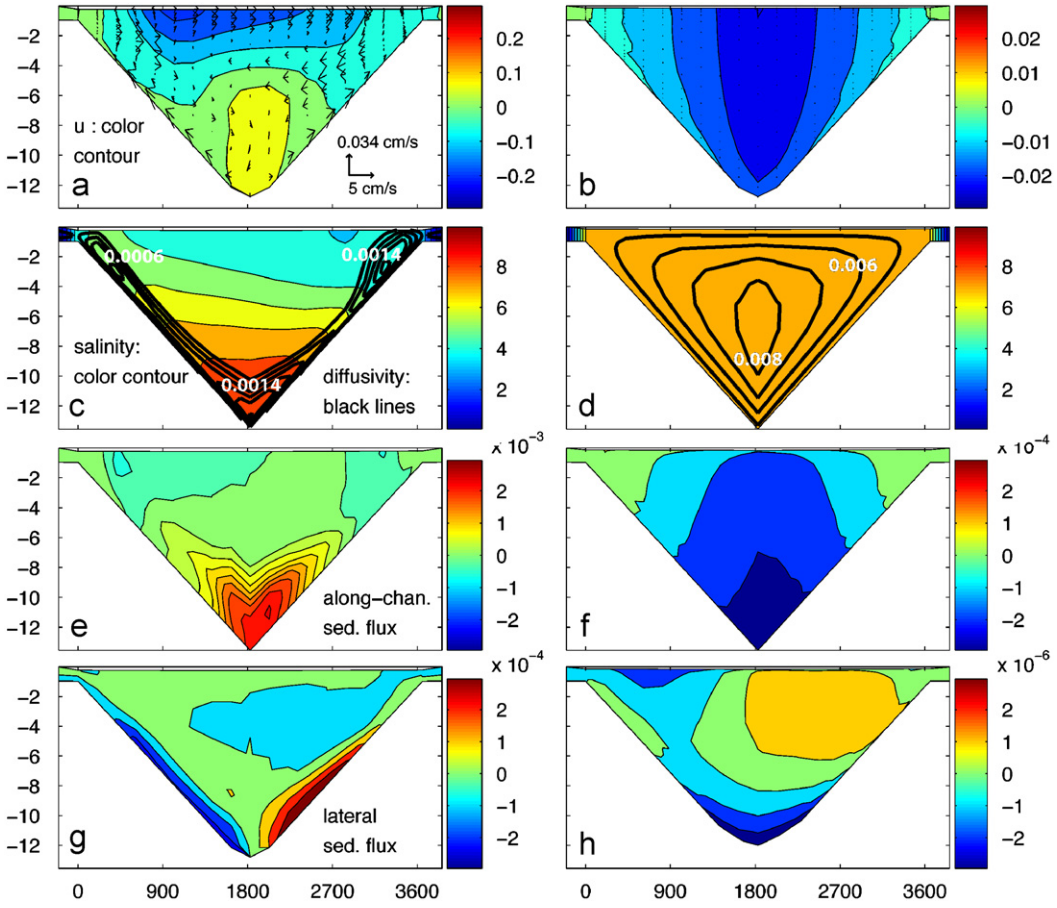

Fig. 9. Cross-sectional profiles of tidally averaged velocity field (a and b; first row), salinity distribution (c and d; second row), longitudinal sediment fluxes (e and f; third row), and lateral sediment fluxes (g and h; forth row) at the locations seaward of salt intrusion (left column) and landward of salt intrusion (right column). These profiles are for the moderately stratified case. Note that color scales on the left and right columns are different. Parts (a) and (e) are 1 order of magnitude bigger than (b) and (f). Part (g) is 2 orders of magnitude bigger than (h). In the second row, distributions of eddy diffusivity, indicated by thick black lines and white fonts, are superposed on top of the salinity distribution (color scale). Tidally averaged salinity landward of salt intrusion (d) is offset by 7.5 psu for better visualization.

(looking seaward), which is opposite to what we expect from Coriolis deflection of the surface flow. This is likely a model artifact caused by the lack of a surface mixed layer (without wind), which results in near surface stratification in the cases presented here. The lateral tilting causes greater suppression of vertical mixing due to stratification on the left shoal and more well-mixed conditions on the right shoal, with correspondingly higher tidally averaged eddy viscosity on the right ($0.0014\,m^2\,s^{-1}$; thick black lines in Fig. 9c). As a result, the tidally averaged along-channel velocity on the right shoal is more affected by friction, while the velocity on the left shoal is much less affected. In real estuaries there is usually a well-defined surface mixed layer. The presence of a surface mixed layer reduces lateral differences in eddy viscosity and thus eliminates the artifact. Increasing water depth also can eliminate this model artifact because it decreases the effects of bottom friction and thus the effects of lateral differences in eddy viscosity on surface flows. Indeed, when we deepen the whole domain by 4 m, a tidally averaged, down-estuary surface flow maximum on the right side is recovered. Most importantly, the lateral circulation pattern remains unchanged after the depth deepening. Hence, the model artifact does not affect the overall lateral dynamics presented here.

Seaward of the salt intrusion, tidally averaged lateral circulation (Fig. 9a) is consistent with up-slope flows driven by boundary mixing near bottom and return flows toward the interior at mid-depth. Near surface, lateral flows toward the right are driven by lateral density gradient set up by isohaline tilting. Influences of Ekman-forced lateral flow are nearly absent because Ekman-forced lateral circulation reverses with tides and thus is largely canceled out after tidal averaging. This cancellation is clearly shown at the cross section landward of salt intrusion where tidally averaged lateral circulation is extremely weak (max v of $0.016\,cm\,s^{-1}$). The residual circulation is clockwise, following the Ekman-forced pattern during ebb because of slightly stronger ebbing currents.

Net along-channel sediment fluxes at the cross sections seaward and landward of the salt intrusion are in opposite directions (Fig. 9e and f). Seaward of the salt intrusion,

there is a strong up-estuary transport of sediments near the bottom because of enhanced resuspension during the flood tide due to the estuarine circulation. Sediment flux in the interior is largely zero because stratification confines suspended sediments close to the bottom. There are relatively weak down-estuary fluxes on the shallow slopes owing to low sediment concentration and weak down-estuary residual flows. Net sediment flux landward of salt intrusion, in contrast, is predominantly down-estuary as anticipated from net down-estuary axial velocity. But this down-estuary flux is one order of magnitude smaller and is uniformly distributed over the water column in the absence of stratification. The weak up-estuary fluxes on the shallow regions are probably due to Stoke's transport. The cross-sectional integrations of net sediment fluxes are about 8.4 and $-2.7\,\mathrm{kg\,s^{-1}}$ seaward and landward of salt intrusion, respectively. These opposite-directed net transports favor the development of an estuarine turbidity maximum zone (ETM) near the salt limit (e.g. Sanford et al., 2001).

Net lateral sediment flux seaward of the salt intrusion is up-slope, leading to net sediment erosion in the channel and net deposition on the shallow slopes (Fig. 9(g)). Net up-slope sediment flux near the bottom is consistent with the residual lateral circulation driven by boundary mixing. The net up-slope flux is higher on the right slope because high sediment concentration in the channel only occurs during flood (Fig. 7a3 and b3) when lateral flows are predominantly toward the right slope (Fig. 7a5 and b5). The net up-slope flux on the right slope gradually decreases and terminates at about 4 m from the surface where the 6 psu isohaline roughly intersects the right slope. This convergence of up-slope flux not only favors sediment accumulation below the halocline on the right slope but also drives net lateral flux from the boundary to the interior which can clearly be seen in the center of Fig. 9g. On the left slope, on the other hand, the net up-slope flux as well as the convergence are weaker because the isohalines are predominantly tilted upward toward the left (Fig. 9c). As a result, we anticipate higher sediment deposition on the right slope.

Contrasting with the patterns seaward of the salt intrusion, net lateral sediment flux landward of salt intrusion is at least 2 orders of magnitude weaker and generally follows the clockwise, net lateral circulation (Fig. 9h). Thus, sediment re-distribution by lateral circulation should be relatively negligible landward of salt intrusion.

Decomposing tidally averaged lateral sediment flux further confirms that preferential transport of sediments toward the right seaward of the salt intrusion is due to tidal asymmetry in sediment resuspension and lateral flows. Depth-integrated, tidally averaged lateral sediment flux (first term) can be decomposed into mean advective (second term) and tidal pumping fluxes (third term) (e.g. Huijts et al., 2006):

$$\underset{(1)}{\int (\overline{v \cdot c})\,\mathrm{d}z} = \underset{(2)}{\int (\bar{v} \cdot \bar{c})\,\mathrm{d}z} + \underset{(3)}{\int (\overline{v' \cdot c'})\,\mathrm{d}z}, \tag{7}$$

where v is lateral flow speed, c is suspended sediment concentration, overbar is tidal average, and prime is tidal variation. As Fig. 10a shows, total transport (first term) is to remove sediments out of the channel and preferentially transport sediments toward the right. The mean advective flux tends to distribute sediments evenly about the channel axis. The pumping flux (all positive) is the one responsible for this net rightward transport. This result is expected because resuspended sediment is mostly available in the channel during flood when lateral flows are mainly toward right (Fig. 7a and b). Bottom sediment distributions after 60 days of model run illustrate the outcome of such transport patterns (solid line in Fig. 10b). There is net erosion (zero means no change from initial state) in the channel. The eroded sediments from the channel preferentially deposit on the right due to stronger lateral sediment flux and the convergence there (around 2500 m). Landward of salt intrusion, on the other hand, bottom sediments remains unchanged (dashed line in Fig. 10b), as anticipated from extremely weak net lateral sediment fluxes.

7. Discussion and conclusions

7.1. How important is the boundary mixing mechanism?

We have shown in Section 4.2 that without Coriolis forcing, an analytical solution for boundary-mixing-driven lateral flow with a 2 h lag agrees reasonably well with model results. We have also demonstrated in Section 4.3 that with Corilois forcing, a linear superposition of boundary-mixing-driven (V_B) and Ekamn-forced lateral flows (V_{E2}) is a good representation of near-bottom lateral flows predicted by the model. These results suggest that boundary mixing can be an important driving mechanism of lateral circulation in stratified estuaries. However, we have not yet considered a third candidate mechanism, differential advection.

For the sake of simplicity and because our focus here is on the boundary mixing mechanism, we consider a system without Coriolis forcing to compare the relative influences of boundary mixing and differential advection. Both boundary mixing and differential advection mechanisms require lateral salinity gradient (s_y) as a driving force. To evaluate this lateral salinity gradient, we look at the tidally varying salt balance:

$$s_t + us_x + vs_y + ws_z = (Ks_z)_z, \tag{8}$$

where s is salinity, (u, v, w) is velocity field, and K is vertical eddy diffusivity. Sub-grid horizontal mixing of salt is set to zero, but the advection scheme itself compensates with mild numerical diffusion. Differentiating Eq. (8) with respect to y yields

$$\underset{(i)}{(s_y)_t} = \underset{(ii)}{-(us_x)_y} - \underset{(iii)}{(vs_y)_y} - \underset{(iv)}{(ws_z)_y} + \underset{(v)}{[(Ks_z)_z]_y}, \tag{9}$$

The first term (i) is the rate of change in lateral salinity gradient, the second term (ii) is the differential advection of

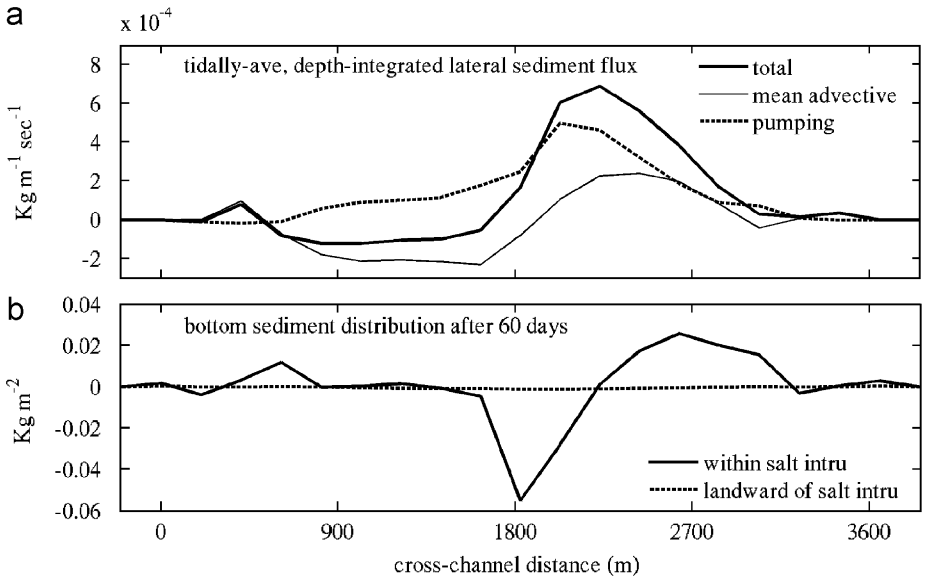

Fig. 10. (a) Decomposition the tidally averaged, depth-integrated lateral sediment transport (thick solid line, $\int(\overline{v}\cdot\overline{c})\,dz$) into mean advective (thin solid line, $\int(\bar{v}\cdot\bar{c})\,dz$) and tidal pumping (dashed, $\int\overline{(v'\cdot c')}\,dz$) components. v and c are lateral flows and suspended sediment concentration, respectively. The overbars denote tidal average, and the primes are tidal variations. (b) Comparison of changes in bottom sediment thickness in the cross-channel direction after 60-day model runs. Positive y-values represent net sediment deposition, whereas negative values represent net erosion. The solid and dashed lines are at the location seaward of and landward of salt intrusion, respectively.

longitudinal salinity gradient by lateral shear, the third term (iii) may be interpreted as lateral compression/decompression of salinity gradient, the fourth term (iv) is the tilting of isohalines, and the fifth term (v) is the lateral variations in the vertical diffusive salt flux gradient, which is associated with boundary mixing. Our focus here is to compare the contribution of differential advection (ii) and boundary mixing (v) to the lateral salinity gradient. Thus, we combine (iii) and (iv) into a collective term: lateral advection. Fig. 11 shows how differential advection, boundary mixing, and lateral advection terms contribute to the rate of change of the lateral salinity gradient. The differential advection term changes sign when tide turns, as expected. All four terms vary with comparable magnitude, suggesting that differential advection, boundary mixing, and lateral advection all contribute to the rate of change in lateral salinity gradient. Note however that the variability in the boundary mixing term is most correlated with the variability in the rate of change of the lateral salinity gradient ($R^2 = 0.6$), especially during flood. Thus, these results support our contention that boundary mixing is an important driving mechanism for lateral circulation in estuaries similar to those modeled here.

Several aspects of the above analysis require further investigation. It is not clear how to separate boundary mixing and differential advection mathematically, as they both contribute to lateral salinity gradients and are associated with each other. Also, the above analysis neglects Coriolis forcing. Ekman veering in the bottom boundary layer can modify lateral salinity gradients by tilting isohalines. This makes distinguishing the mechanisms associated with lateral salinity gradient even more complicated. Huijts et al. (2006) presented an analytical model to evaluate relative contributions from differential advection and Coriolis forcing. Due to a prescribed salinity gradient, their model may be more useful for vertically mixed systems. For more stratified systems in which the lateral salinity gradient varies spatially and temporarily, an analytical solution including all three mechanisms has not been documented in the literature. Finally, though we found in Section 4.3 that linearly superposing boundary-mixing-driven and Ekman-forced lateral flows is a good representation of the near-bottom lateral flows predicted by the model, the validity of linear superposition across different estuarine systems (especially under weaker stratification) requires further verification.

7.2. Evidence of boundary mixing in the literature

As mentioned in Section 1, there are very few reports in the literature about boundary mixing on slopes in estuaries. Several cross-sectional snapshots reported by Phillips et al. (1986) from a dye injection study are consistent with boundary-mixing-driven flow and salt structure, but their conclusion is not definitive. Lerczak and Geyer (2004) reported that lateral circulation driven by boundary mixing was relatively weak compared with differential advection in their modeling study, which contradicts our findings here. The discrepancy may be due to their use of a constant eddy viscosity/diffusivity. In model runs with similar top–bottom salinity differences to ours, their eddy viscosities are 5.4 and $3.3\times10^{-4}\,m^2\,s^{-1}$, while our values solved by the k–ε closure are roughly 1–2 and $0.5-1\times10^{-3}\,m^2\,s^{-1}$ within 3 m above the bottom for moderately and highly stratified cases, respectively. Therefore, in their model runs, boundary mixing is much weaker, which then leads to

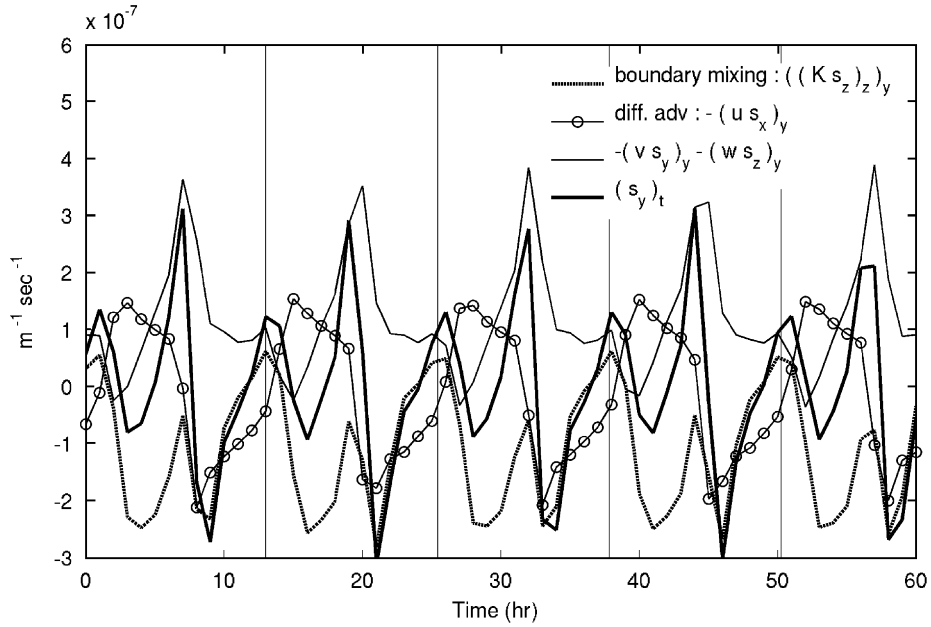

Fig. 11. Comparisons of the relative contribution from boundary mixing (dashed), differential advection (circle), and lateral advection (thin solid line) to the change rate of lateral salinity gradient (thick solid line; $(s_y)_t$). The Coriolis forcing is turned off, as in Fig. 4a (moderately stratified). Each term is an average of the bottom 2 m of the water column over all cross-channel locations where the total depth is over 4 m, on the right side of the channel. The vertical lines are about 2 h after maximum flood.

insignificant lateral flows driven by boundary mixing. This speculation is further confirmed in Fig. 16 of their paper. When they used a modern turbulence closure, isohalines perpendicular to the slopes and the resulting up-slope flows were much clearer.

A field observation from the Hudson River estuary may provide support for boundary-mixing-driven lateral circulation. Lerczak and Geyer (2004) reported that the differential advection mechanism cannot explain the observed vertical profile of lateral flow during neap tides in the Hudson River estuary (Fig. 12a). The vertical profile taken at a location on the right of the channel (looking seaward) shows a three-layer structure during maximum flood and weaker lateral flows during maximum ebb. The vertical profile of lateral flows from our model (Fig. 12b) shows very similar patterns during maximum flood. The three-layer structure during maximum flood results from the peak Ekman-forced flow enhancing the boundary-mixing-driven flow toward the right slope near bottom and the return flows toward the left at mid-depth. In contrast, during maximum ebb these two flows are against each other, leading to weaker lateral flows. Although the model and the observations from the Hudson are not directly comparable as bathymetry and forcings are different, the high degree of similarity in lateral flow structure during flood leads us to speculate that boundary mixing may drive significant amount of lateral flows under stratified conditions.

One possible reason that boundary mixing has received little attention in the estuarine literature is the required high vertical resolution in the bottom boundary layer. As shown in Fig. 7, boundary layer height is at most 2–3 m, and strong boundary-mixing-driven flows are in the lower part of the boundary layer. Another reason may be that boundary mixing is highly time-dependent. We have shown in Figs. 5 and 6 that boundary-mixing-driven flows oscillate with tides and peaks after maximum floods and ebbs. This unsteadiness and the resulting phase differences with other mechanisms, such as Ekman-forced flow, may hinder efforts to distinguish boundary mixing. Relatively steady forcing is probably why reports of boundary mixing are mainly on continental shelves (e.g. Weatherly and Martin, 1978; Lentz and Trowbridge, 1991). Observations with high spatial and temporal resolution are thus required to explore and distinguish the role of boundary mixing on lateral dynamics in stratified estuaries.

7.3. Phase lag between model results and analytical solution for boundary mixing

A relevant time scale that influences boundary mixing is the diffusive time scale. The diffusive time scale controls the speed with which vertical mixing modifies the density field, which in turn drives the lateral circulation. Given boundary layer heights δ around 3 and 2 m (Fig. 4b and c) and averaged eddy diffusivity within the boundary layer K_z about 1.5×10^{-3} and 0.75×10^{-3} for moderately and highly stratified cases, respectively, the corresponding diffusive time scales (δ^2/K_z) are about 1.7 and 1.5 h. These values are consistent with the 2-h lag between the steady state analytical solution for boundary mixing and the model prediction (Fig. 5b). However, the 2 h lag may also be influenced by other processes, such as tidal acceleration/deceleration. Further investigation is needed.

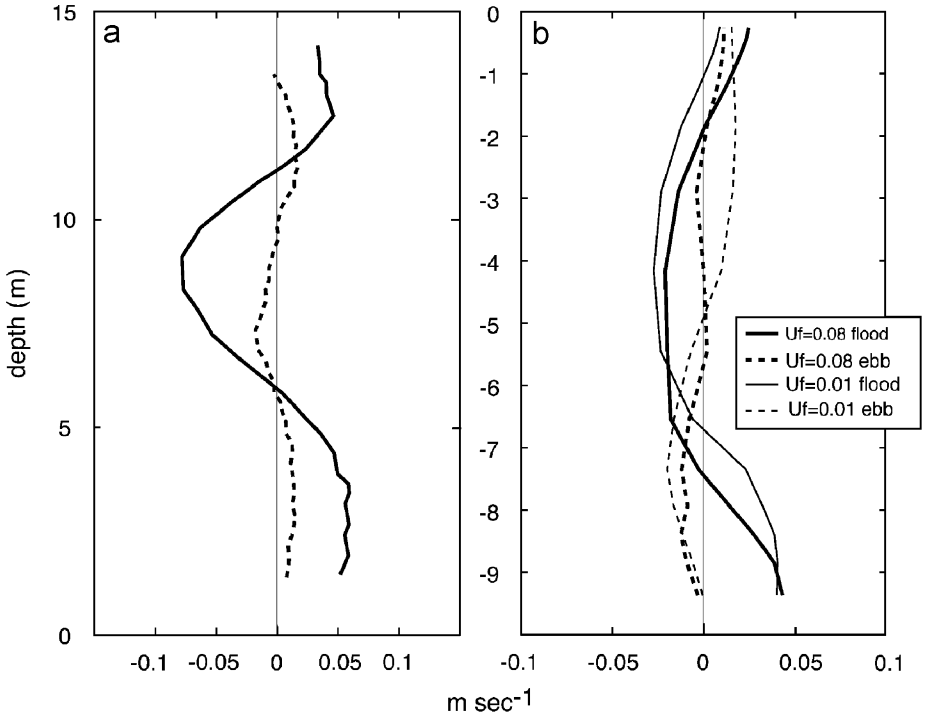

Fig. 12. Vertical profiles of lateral flows at an off-channel location (a) observed in the Hudson River estuary during neap tides at maximum flood (solid) and ebb (dashed) and (b) from the model. (a) is reproduced from Fig. 15 in Lerczak and Geyer (2004). In (b), thick and thin lines separate highly stratified and moderately stratified cases. The solid and dashed lines are at maximum flood and ebb, respectively.

In the two-layer time-dependent Ekman model (Section 4.3), there is a phase difference between the upper layer axial flow and all other flow components (Eq. (5a) vs. Eqs. (5b)–(5d)). This phase difference results from the linearized bottom friction parameter R, which affects the lower layer axial flow and lateral flow in both layers as a result. Thus, even though the Ekman model does not resolve the details of vertical mixing in the bottom boundary layer, a phase lag associated with bottom friction is built into the solution. The time scale of this phase lag is $1/R$, approximately 2.5 h for the cases presented here. So, from a dynamics standpoint, it is appropriate to compare the direct output of the time-dependent Ekman layer model to the lagged output of the steady state boundary-mixing model.

7.4. Deficiencies of the model

The model-predicted salinity fields lack well-defined haloclines. The stratification in Fig. 7 is mostly linear from top to bottom. A diffused halocline also appears in realistic estuarine simulations (Li et al., 2005; Warner et al., 2005a). Such pattern contrasts with the sharp halocline that is often found during highly stratified conditions in real estuaries (e.g. the Hudson; Lerczak and Geyer, 2004). One possible reason for the lack of sharp halocline in our model is related to poor parameterization of interior mixing in the turbulence closures. Internal mixing processes are approximated by a constant and rather high background diffusivity of $8\times10^{-5}\,m^2\,s^{-1}$ here. Although using a lower background diffusivity of $5\times10^{-6}\,m^2\,s^{-1}$ sharpens the halocline, it also results in an unrealistic salt intrusion length under the desired tidal currents and freshwater discharge. Adjusting the background diffusivity to simulate damping by stratification (North et al., 2004) is one possible approach for sharpening the halocline. It is also possible that parameterizing the effects of wind stirring and surface wave breaking, which likely contribute to significant upper layer mixing may, lead to more realistic salt structure.

Another limitation of our model is the rather simple bathymetry. Although a triangular shape is more generic than a rectangular one, many coastal plain estuaries feature a gentle shoal and a sharply incised channel. In other words, the angle of the slope changes across the estuary instead of being constant. This laterally varying slope angle can cause local convergence/divergence of boundary-mixing-driven lateral flows and thus complicate the lateral dynamics. The role of boundary mixing under more realistic cross-sectional profiles and different slope angles will be addressed in the future.

7.5. Implications for estuarine morphology

The bottom sediment distribution seaward of the salt intrusion after a 60-day model run shows net erosion in the channel and net deposition preferentially on the right slope (Fig. 10b; looking seaward). The net erosion is due to constant up-slope transport of sediments by boundary-mixing-driven flows from the channel. The preferential

deposition on the right is mainly due to tidal asymmetry in sediment resuspension and lateral flows (dashed line in Fig. 10a; see Section 6.2). Such erosion/deposition patterns over a long time would favor a shallow shoal on the right and the deep channel shifted closer to the left. The resulting axially asymmetrical channel profile is consistent with commonly observed profiles in shallow, coastal plain estuaries, such as the Hudson River estuary, James and York River estuary, and the main stem of Chesapeake Bay (e.g. Geyer et al., 1998; Kerhin et al., 1988). However, the net erosion in the channel predicted by the model contradicts the observed fast deposition there in estuaries like Chesapeake Bay (Hobbs et al., 1992). This discrepancy may result from the dominance of channel-directed sediment transport during storms when strong wind-wave forcing leads to high resuspension on the shoals (Sanford, 1994). Other factors that are not considered here including wind forcing, laterally and longitudinally varying bathymetry, and limited sediment supply in mud pools can complicate the lateral dynamics of suspended sediment transport and thus merit further investigation.

Acknowledgments

We thank the ROMS user community. The original manuscript is much improved because of the efforts from two anonymous reviewers. S.N.C thanks Parker MacCready, Rocky Geyer, and James Lerczak for many insightful discussions. S.N.C gratefully acknowledges support from a Maryland Sea Grant Fellowship and ONR grant no. A100497 (CSTM). LPS was supported by NSF grant nos. OCE-0536466 (MUDBED) and OCE-0453905 (BITMAXii), and ONR grant no. A100497 (CSTM). This is UMCES publication no. 4141.

References

Burchard, H., Baumert, H., 1998. The formation of estuarine turbidity maxima due to density effects in the salt wedge. A hydrodynamic process study. Journal of Physical Oceanography 28, 309–321.

Canuto, V.M., Howard, A., Cheng, Y., Dubovikov, M.S., 2001. Ocean turbulence I: one-point closure model-Momemtun and heat vertical diffusivities. Journal of Physical Oceanography 31, 1413–1426.

Chant, R.J., Wilson, E., 1997. Secondary circulation in a highly stratified estuary. Journal of Geophysical Research 102, 23207–23216.

Dyer, K.R., 1997. Estuaries: A Physical Introduction. Wiley, Chichester; NY, 195pp.

Fischer, H.B., 1972. Mass transport mechanisms in partially stratified estuaries. Journal of Fluid Mechanics 53, 671–687.

Fugate, D.C., Friedrichs, C.T., Sanford, L.P., 2007. Lateral dynamics and associated transport of sediments in the upper reaches of a partially mixed estuary, Chesapeake Bay, USA. Continental Shelf Research 27, 679–698.

Garrett, C., MacCready, P., Rhines, P.B., 1993. Boundary mixing and arrested Ekman layers: rotating stratified flow near a sloping boundary. Annual Review of Fluid Mechanics 25, 291–323.

Geyer, W.R., Signell, R.P., Kineke, G.C., 1998. Lateral Trapping of Sediment in a Partially Mixed Estuary. Physics of Estuaries and Coastal Seas, Balkema.

Geyer, W.R., Trowbridge, J.H., Bowen, M.M., 2000. The dynamics of a partially mixed estuary. Journal of Physical Oceanography 30, 2035–2048.

Haidvogel, D.B., Arango, H.G., Hedstrom, K., Beckmann, A., Malanotte-Rizzoli, P., 2000. Model evaluation experiments in the North Atlantic basin: simulations in nonlinear terrain-following coordinates. Dynamics of Atmospheres and Oceans 32, 239–281.

Hobbs, C.H., Halka, J.P., Kerhin, R.T., Carron, M.J., 1992. Chesapeake Bay sediment budget. Journal of Coastal Research 8 (2), 292–300.

Huijts, K.M.H., Schuttelaars, H.M., De Swart, H.E., Valle-Levinson, A., 2006. Lateral trapping of sediment in tidal estuaries: an idealized model study. Journal of Geophysical Research 111, C12016.

Huzzey, L.M., Brubaker, J.M., 1988. The formation of longitudinal fronts in a coastal estuary. Journal of Geophysical Research 93, 1329–1334.

Johnson, G.C., Ohlsen, D.R., 1994. Frictionally modified rotating hydraulic channel exchange and ocean outflows. Journal of Physical Oceanography 24, 66–78.

Jones, W.P., Launder, B.E., 1972. The prediction of laminarization with a two-equation model of turbulence. International Journal of Heat and Mass Transfter 15, 301–314.

Kalkwijk, J.P.T., Booij, R., 1986. Adaptation of secondary flow in nearly-horizontal flow. Journal of Hydraulic Engineering 24, 19–37.

Kassi, A., Hill, A.E., Fujiwara, T., Simpson, J.H., 2000. Effect of the Earth's rotation on the circulation in regions of freshwater influence. Journal of Geophysical Research 105 (C7), 16961–16970.

Kerhin, R., Halka, J., Wells, D.V., Hennessee, E.L., Blakelee, P.J., Zoltan, N., Cuthbertson, R.H., 1988. The Surficial Sediments of Chesapeake Bay, Maryland: Physical Characteristics and Sediment Budget, vol. 48. Maryland Geological Survey, Baltimore.

Lentz, S.J., Trowbridge, J.H., 1991. The bottom boundary layer over the northern California shelf. Journal of Physical Oceanography 21, 1186–1201.

Lerczak, J.A., Geyer, W.R., 2004. Modeling the lateral circulation in straight, stratified estuaries. Journal of Physical Oceanography 34, 1410–1428.

Li, C., O'Donnell, J., 1997. Tidally driven residual circulation in shallow estuaries with lateral depth variation. Journal of Geophysical Research 102, 27915–27929.

Li, C., Valle-Levinson, A., 1999. A two-dimensional analytic tidal model for a narrow estuary of arbitrary lateral depth variation: the intertidal motion. Journal of Geophysical Research 104, 23525–23543.

Li, M., Zhong, L., Boicourt, W.C., 2005. Simulations of Chesapeake Bay estuary: sensitivity to turbulence mixing parameterizations and comparison with observations. Journal of Geophysical Research 110, C12004.

MacCready, P., Rhines, P.B., 1993. Slippery bottom boundary layer on a slope. Journal of Physical Oceanography 23, 5–22.

Marchesiello, P., McWilliams, J.C., Shchepetkin, A., 2001. Open boundary conditions for long-term integration of regional ocean models. Ocean Modelling 3, 1–20.

Martin, W., MacCready, P., Dewey, R., 2005. Boundary layer forcing of a semidiurnal cross-channel seiche. Journal of Physical Oceanography 35, 1518–1537.

Mied, R.P., Handler, R.A., Donato, T.F., 2002. Regions of estuarine convergence at high Rossy number: a solution in estuaries with elliptical cross sections. Journal of Geophysical Research 107.

North, E.W., Chao, S.-Y., Sanford, L.P., Hood, R.R., 2004. The influence of wind and river pulses on an estuarine turbidity maximum: numerical studies and field observations. Estuaries 27 (1), 132–146.

Nunes, R.A., Simpson, J.H., 1985. Axial convergence in a well-mixed estuary. Estuarine, Coastal, and Shelf Science 20, 637–649.

Ott, M.W., Garrett, C., 2002. Frictional estuarine flow in Juan de Fuca Strait with implications for secondary circulation. Journal of Geophysical Research 103, 15657–15666.

Phillips, O.M., 1970. On flows induced by diffusion in a stably stratified fluid. Deep Sea Research 17, 435–443.

Phillips, O.M., Shyu, J., Salmun, H., 1986. An experiment on boundary mixing: mean circulation and transport rates. Journal of Fluid Mechanics 173, 473–499.

Sanford, L.P., 1994. Wave-forced resuspension of upper chesapeake bay muds. Estuaries 17 (1B), 148–165.

Sanford, L.P., Halka, J.P., 1993. Assessing the paradigm of mutually exclusive erosion and deposition of mud, with examples from upper Chesapeake Bay. Marine Geology 114 (1/2), 37–57.

Sanford, L.P., Suttles, S.E., Halka, J.P., 2001. Reconsidering the physics of the Chesapeake Bay estuarine turbidity maximum. Estuaries 24 (5), 655–669.

Smith, R., 1980. Bouyancy effects upon longitudinal dispersion in wide well-mixed estuaries. Philosophical Transactions of the Royal Society of London. Series A. Mathematical and Physical Sciences 296, 467–496.

Trowbridge, J.H., Lentz, S.J., 1991. Asymmetric behavior of an oceanic boundary layer above a sloping bottom. Journal of Physical Oceanography 21, 1171–1185.

Valle-Levinson, A., Li, C., Wong, K.C., Lwiza, K.M.M., 2000. Convergence of lateral flow along a coastal plain estuary. Journal of Geophysical Research 105, 17045–17061.

Warner, J.C., Geyer, W.R., Lerczak, J.A., 2005a. Numerical modeling of an estuary: a comprehensive skill assessment. Journal of Geophysical Research 110, C05001.

Warner, J.C., Sherwood, C.R., Arango, H.G., Signell, R.P., 2005b. Performance of four turbulence closure models implemented using a generic length scale method. Ocean Modeling 8, 81–113.

Weatherly, G.L., Martin, P.J., 1978. On the structure and dynamics of the oceanic bottom boundary layer. Journal of Physical Oceanography 8, 557–570.

Woodruff, J.D., Geyer, W.R., Sommerfield, C.K., Driscoll, N.W., 2001. Seasonal variation of sediment deposition in the Hudson River estuary. Marine Geology 179, 105–119.

Wunsch, C., 1970. On oceanic boundary mixing. Deep Sea Research 17, 293–301.